The Astrophysical Journal, 914:13 (13pp), 2021 June 10 https://doi.org/10.3847/1538-4357/abf82d

Ultradense Gas Tracked by Unshifted Broad Absorption Lines in a Quasar

Qiguo Tian[1,2], Xiheng Shi[1,2], Lei Hao[3], Yipeng Zhou[3], Zhenzhen Li[3], Peng Jiang[1,2], Shengmiao Wu[1,2], Chenwei Yang[1,2], Shaohua Zhang[1,2,4], and Hongyan Zhou[1,2,5]

[1] Polar Research Institute of China, 451 Jinqiao Road, Pudong, Shanghai 200136, People's Republic of China; zhouhongyan@pric.org.cn, tianqiguo@pric.org.cn

[2] MNR Key Laboratory for Polar Science, Polar Research Institute of China, 451 Jinqiao Road, Shanghai 200136, People's Republic of China

[3] Key Laboratory for Research in Galaxies and Cosmology, Shanghai Astronomical Observatory, Chinese Academy of Science, 80 Nandan Road, Shanghai 200030, People's Republic of China; haol@shao.ac.cn

[4] Shanghai Key Lab for Astrophysics, Shanghai Normal University, 200234, Shanghai, People's Republic of China

[5] Key laboratory for Research in Galaxies and Cosmology of Chinese Academy of Science, Department of Astronomy, University of Science and Technology of China, Hefei, Anhui 230026, People's Republic of China

Received 2020 September 22; revised 2021 April 13; accepted 2021 April 13; published 2021 June 9

Abstract

We present a detailed analysis of the broad absorption line system in the quasar SDSS J122017.06+454941.1, which are clearly detected in hydrogen Lyman series and metal lines, such as C IV, Si IV, Si III, Al III, and C II, with a similar velocity as that of the broad emission lines. We reliably measured the column densities of H I, Al III, and C II, and obtained a low limit to Si IV and Si III. With the help of the photoionization simulations, we found that the absorption gas has a hydrogen number density $n_{\rm H} \approx 10^{11.03}\,{\rm cm}^{-3}$ and a hydrogen column density $N_{\rm H} \approx 10^{21.0}\,{\rm cm}^{-2}$, and is exposed to the radiation with an ionization parameter $U \approx 10^{-1.25}$, and thus located the absorber at ~0.3 pc from the central supermassive black hole, remarkably similar to the radius of the broad-line region (BLR; 0.17–0.84 pc as estimated by the luminosity–radius relation) of the quasar. It is likely that our line of sight may happen to intercept the low-column part of the BLR with a high density similar to that of the inferred value of the absorber. We suggest that detection of Al III absorption line doublet in moderate quality quasar spectra could be a good indicator of dense gases, provided that the neutral hydrogen column density of the absorber is $15.4 \lesssim \log N_{\rm H\,I}\,({\rm cm}^{-2}) \lesssim 16.5$.

Unified Astronomy Thesaurus concepts: Broad-absorption line quasar (183); Quasars (1319); Active galactic nuclei (16)

1. Introduction

Active galactic nuclei (AGNs), observed as stellar-like point sources and powered by accretion onto supermassive black holes (BHs), are extraordinary luminous objects at the centers of galaxies (e.g., Lynden-Bell 1969; Rees 1984; Hopkins et al. 2006). High-density gas on a sub-parsec scale, next to the active BHs in the centers of AGNs, has drawn substantial attention in recent years (e.g., Netzer 2013, 2020). The broad-line region (BLR) has a clear view of the vicinity of BHs (e.g., Elvis 2000; Netzer 2015), and the broad emission lines from the region are the most recognized features in AGN spectra. The gas in the BLR is often of high density. The lower limit on the density of BLR gas, determined from the weakness of certain metastable and semi-forbidden lines that are relatively more prominent in lower-density gases (e.g., $n_{\rm H} \sim 10^3\,{\rm cm}^{-3}$ in narrow line region, Peterson 1993) is about $n_{\rm H} = 10^{9-10}\,{\rm cm}^{-3}$, where $n_{\rm H}$ is the hydrogen number density. The upper limit on the density is not well determined and densities as high as $10^{13}\,{\rm cm}^{-3}$ have been proposed (e.g., Matsuoka et al. 2008; Negrete et al. 2012; Panda et al. 2018).

The kinematics and geometry of BLR gas have been extensively studied by reverberation mapping (RM, e.g., Peterson 1993). The broad emission line fluxes are observed to vary in response to the continuum variations, with a short (usually days to weeks for typical Seyfert 1 galaxies) time delay that is attributable to the light travel time across the BLR (e.g., Peterson 2006). Thus, by measuring the delay of the variations of the broad emission lines compared to the continuum, one can estimate the location and geometry of the BLR. Another method to study the BLR, which we use in this paper, is through the absorption lines. This might be a bit unexpected, as the broad emission lines are the most prominent features in AGN spectra, and BLR gas only fills a small fraction (10^{-7} to ~0.1) of the total volume of the BLR (Schneider 2015). However, once the BLR gas clouds are in our line of sight, it produced absorption lines, as have been observed recently in the quasar PG 1411+442 (Hamann et al. 2019).

The study on absorption lines in quasars by itself has a long history and involves voluminous literature accumulated ever since its discovery (Lynds 1967). Broad absorption lines (BALs) are typical observational features in the AGN spectra. They are often referred to as a continuous absorption trough covering a large range of velocities from $-2000\,{\rm km\,s^{-1}}$ by definition (Weymann et al. 1991) up to several times of $10^4\,{\rm km\,s^{-1}}$. BALs are also divided as in high-ionization BALs (HiBALs) and low-ionization BALs (LoBALs) (e.g., Weymann et al. 1991; Hall et al. 2002; Hamann & Sabra 2004), according to the type of absorption features observed. Typically, HiBAL quasar spectra exhibit absorption lines of C IV, N V, Si IV and O VI, and LoBAL spectra show not only HiBALs, but also the absorption troughs of Mg II, Al III, and C II, etc. (e.g., Liu et al. 2015).

BALs provide abundant diagnostics for the physical conditions of AGN absorbers. Theoretically, the ion column densities and covering factor can be derived when two or more absorption lines from the same lower level can be measured (e.g., Hamann et al. 1997; Arav et al. 2005; Leighly et al. 2011). In practice, Mg II, Al III, Si IV, C IV, C II, and He I* BALs have all been used jointly to constrain the properties of the absorber (e.g., Leighly et al. 2011; Ji et al. 2015; Liu et al. 2016; Tian et al. 2019). As the most abundant element in the universe, hydrogen absorption is another powerful diagnostic. It has been shown that the BALs of Balmer series are useful to constrain the gas densities (e.g., Shi et al. 2016a, 2016b; Zhou et al. 2019). The absorption lines of Lyman series, if they can be observed, can also be used jointly with HiBALs/LoBALs for diagnostics, as they cover wide ranges in the wavelength and oscillator strengths.

Despite numerous efforts, the understanding of the basic properties of the AGN absorbers, especially their locations are still limited (e.g., Hamann et al. 2019). Absorbers at distances varied from the Galactic scale (e.g., Borguet et al. 2012a; Finn et al. 2014; Miller et al. 2018; Xu et al. 2018; Hamann et al. 2019; Tian et al. 2019, and references therein) to parsec or dozens of parsecs scale (e.g., Zhang et al. 2015; Liu et al. 2016; Shi et al. 2016a, 2016b; Veilleux et al. 2016) have all been reported. The reported hydrogen number density range is correspondingly from $n_{\rm H} < 10^4\,{\rm cm}^{-3}$ to $n_{\rm H} > 10^5\,{\rm cm}^{-3}$. The absorbers from much higher hydrogen density, similar to the BLR gas, is also expected. Elvis (2000) suggested that the absorber can be an outflowing wind that is arising vertically from a narrow range of radii on an accretion disk at BLR velocities and then accelerated by the radiation force and bended to the line of sight. The simulations (Risaliti & Elvis 2010) show that, in some cases, the wind cannot achieve a high enough acceleration to reach the escape velocity. The properties of such outflowing gas are mainly of high $n_{\rm H}$, located closely to the central BHs, which were similar to the photoionization simulations carried out by Różańska et al. (2014).

In this paper, we show that when the column density of the neutral hydrogen gas is low, the appearance of Al III absorption puts strong constraints on the density of the absorbing gas into the high-density regime, close to the density expected for the BLR of AGNs. We show this via a photoionization modeling in the next subsection.

1.1. Implication of Joint Using of H I and Al III BALs

If we can detect the Al III absorption lines in a quasar hosting H I Lyman absorptions, it indicates that the optical depth at the deepest point of the Al III trough is within the range of 0.05–3 (in this case, the corresponding normalized residual flux, $e^{-\tau}$, is 0.95–0.05 in the absorption trough), so that the line is neither too weak nor severely saturated (Zhou et al. 2019). Assuming a Gaussian velocity profile (FWHM = 1000 km s^{-1}), the measurable column density of Al III is therefore $1.94 \times 10^{13}\,{\rm cm}^{-2} < N_{\rm Al\,III} < 1.16 \times 10^{15}\,{\rm cm}^{-2}$, which enables measurement of column density over about two orders of magnitude. We then carried out systematic photoionization simulations using Cloudy to study the diagnostic power by combining the information of $N_{\rm H\,I}$ and $N_{\rm Al\,III}$. We assume a slab-shaped, homogeneous gas with solar abundance and spectral energy distribution (SED) consisting of a blackbody big bump with a temperature of 1.5×10^5 K (see details in Section 4.1), hereafter denoted as 4B SED. The simulations were run over $-4 \leqslant \log U \leqslant 4$ and $0 \leqslant \log n_{\rm H}\ ({\rm cm}^{-3}) \leqslant 15$. For each ($U$, $n_{\rm H}$), $N_{\rm H}$ and $N_{\rm Al\,III}$ were recorded when the predicted $N_{\rm H\,I}$ reached a given value (e.g., observed one). The $N_{\rm Al\,III}$ contour distributions for different $N_{\rm H\,I}$, varied from $10^{15.4}$ to $10^{16.9}\,{\rm cm}^{-2}$, are plotted as black dotted lines in Figure 1. Also included in this figure are the $N_{\rm H}$ distribution contours. As has been illustrated, if the Al III absorption line is detected, it indicates that the column density of Al III is within the range of $1.94 \times 10^{13}\,{\rm cm}^{-2} < N_{\rm Al\,III} < 1.16 \times 10^{15}\,{\rm cm}^{-2}$. We denote this range as cyan regions in Figure 1. It can be seen that in the case when $N_{\rm H\,I}$ is relatively low at $15.4 \leqslant \log N_{\rm H\,I}\ ({\rm cm}^{-2}) \leqslant 16.5$, if the Al III absorption line can still be detected, the absorbing gas should be of high density ($n_{\rm H} > 10^{10}\,{\rm cm}^{-3}$). Such a high $n_{\rm H}$ is similar to that of the gas in the BLR, where the density is probably close to $10^{11}\,{\rm cm}^{-3}$.

The reason why the density ($n_{\rm H}$) can be diagnosed by combining the information of $N_{\rm H\,I}$ and $N_{\rm Al\,III}$ is that H^0 and Al^{2+} have dramatically different ionization potentials, thus their ionization structures have very different dependences on the parameters, including the absorbing gas density. To illustrate this better, we show how the parameters of the absorbing gas vary in two models. One is with low density ($n_{\rm H} = 10^4\,{\rm cm}^{-3}$) and the other is with high density ($n_{\rm H} = 10^{12}\,{\rm cm}^{-3}$). Both models have the same U at $\log U = -1$. In Figure 2, we plot the ionic column densities of Al^{2+} and H^0 as functions of $N_{\rm H}$. The dashed and solid curves represent the models of low ($n_{\rm H} = 10^4\,{\rm cm}^{-3}$) and high ($n_{\rm H} = 10^{12}\,{\rm cm}^{-3}$) densities, respectively. It can be seen that the $N_{\rm H^0}$ are significantly different between the low- and high-density models, starting as early as $N_{\rm H} \approx 10^{21}\,{\rm cm}^{-2}$. The difference becomes even more prominent when the gas transfers from the ionized (H II) zone to the neutral (H I) zone. In the low-density case, this transfer occurs at $N_{\rm H} \approx 10^{22}\,{\rm cm}^{-2}$, while in the high-density case, the transfer occurs at $N_{\rm H} \approx 10^{23.3}\,{\rm cm}^{-2}$. Intriguingly, the difference is remarkable even in the ionized zone, at a given $N_{\rm H}$, $N_{\rm H^0}$ in the case of $n_{\rm H} = 10^{12}\,{\rm cm}^{-3}$ is lower than that in case of $n_{\rm H} = 10^4\,{\rm cm}^{-3}$. Therefore, the total hydrogen column density measured at, e.g., $N_{\rm H^0} = 10^{16.6}\,{\rm cm}^{-2}$ is $N_{\rm H} = 10^{21.1}\,{\rm cm}^{-2}$ when $n_{\rm H} = 10^4\,{\rm cm}^{-3}$, but $N_{\rm H} = 10^{21.7}\,{\rm cm}^{-2}$ when $n_{\rm H} = 10^{12}\,{\rm cm}^{-3}$. Since $N_{\rm Al^{2+}}$ as function of $N_{\rm H}$ varies little from low density to high density at around $N_{\rm H} \approx 10^{21} \sim 10^{23}\,{\rm cm}^{-2}$, the same $N_{\rm H^0}$ value would introduce very different $N_{\rm Al^{2+}}$ values. Thus, the combination of Al III and H I might be a robust diagnostic for the gas density. We note that the above analysis is for models with a fixed value of $\log U = -1$ and is for illustration purpose only. The real solution will require the full modeling that surveys the values of parameters, including U, which is shown in Figure 1.

We experimented with other SEDs as inputs to our models, including MF87 (Mathews & Ferland 1987) and HE0238 (Arav et al. 2013). We also tried different metallicities for different SEDs, using both solar ($1.0\,Z_\odot$) and super-solar metallicities (3.0 and $10.0\,Z_\odot$). Different SEDs with the same metallicity give very similar results. For models with the HE0238 and MF87 SEDs and the solar metallicity, it is found that if the $N_{\rm H\,I}$ is in the range of log $N_{\rm H\,I}\,({\rm cm}^{-2}) \sim$ [15.4, 16.7] and [15.4, 17.0], and if the Al III absorption line is detected, the inferred gas density would be $n_{\rm H} > 10^{10}\,{\rm cm}^{-3}$. We get similar results for other models with different metallicities. That is, if the log $N_{\rm H\,I}\,({\rm cm}^{-2})$ values range at [15.1, 16.3], [15.0, 16.3], and [15.2, 16.6] for $3.0\,Z_\odot$ metallicity and [14.7, 15.8], [14.7, 15.8], and [14.9, 16.1] for $10.0\,Z_\odot$ metallicity, with the 4B SED, HE0238 SED, and MF87 SED, respectively, the inferred gas density would also be $n_{\rm H} > 10^{10}\,{\rm cm}^{-3}$ if the Al III absorption line is detected. In what follows in this paper, we use the 4B SED model.

Thus, it would be interesting to launch a systematic search for BAL quasars that show detectable Al III absorption lines, while the H I absorption is not too strong. We carried out such a search from the 12th data release of the Sloan Digital Sky Survey (SDSS DR12; Dawson et al. 2013), with two criteria: (1) redshift $3.0 < z < 4.47$ and (2) spectral signal to noise ratio (S/N > 20). Al III absorption lines were visually detected in 19 sources, among which SDSS J122017.06+454941.1 (hereafter SDSS J1220+4549) had the highest spectral quality, and we

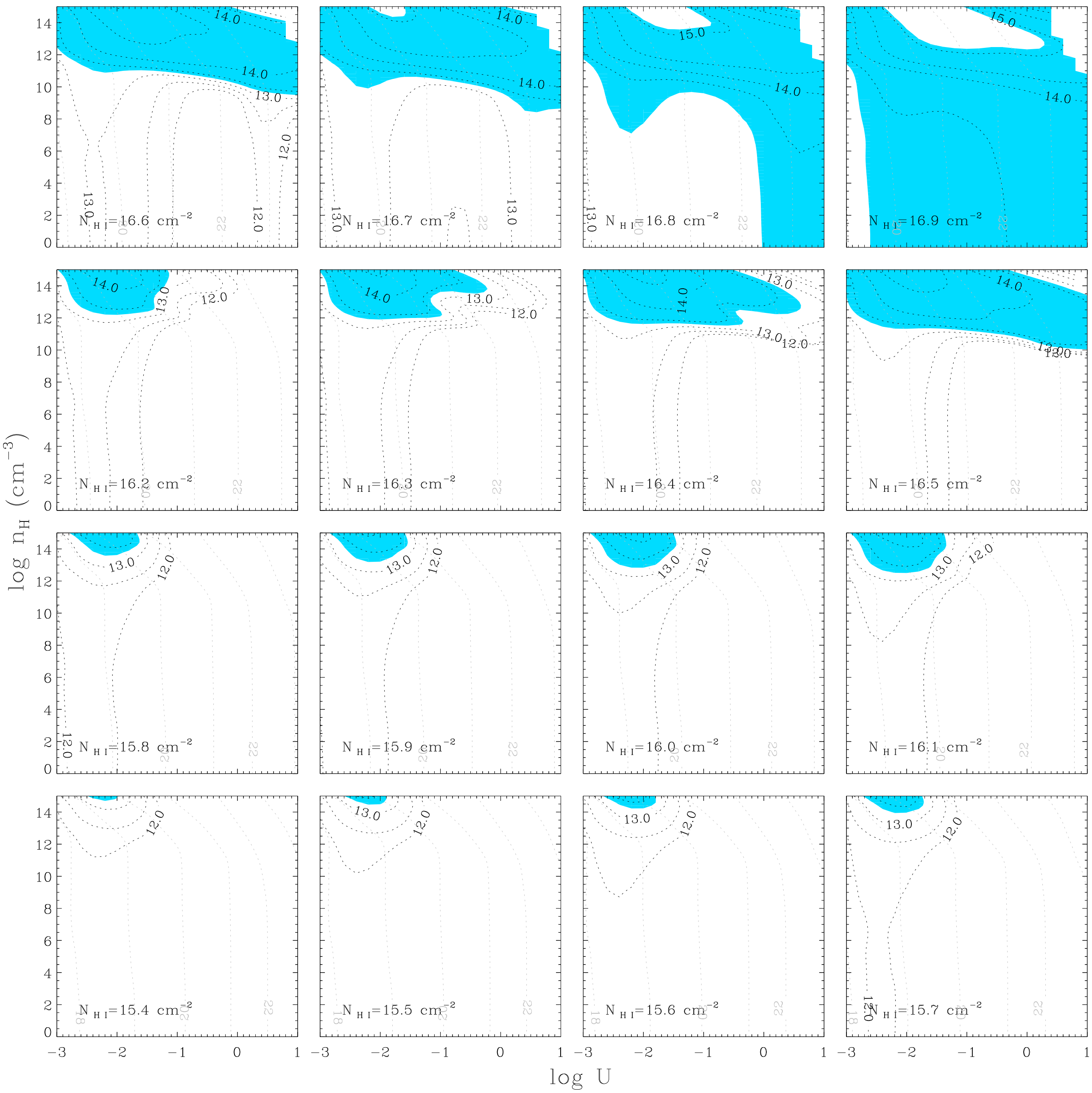

Figure 1. Sensitive range of Al III λ1854.72 BAL with log $N_{\mathrm{H\,I}}$ (cm^{-3}) varied from 15.4–16.9 in a step length of 0.1 dex. The black dotted lines are the contours of Al III column density. Assuming a Gaussian velocity dispersion (FWHM = 1000 km s^{-1}), Al III λ1854.72 is considered to be sensitive in measuring the ionic column density as long as the optical depth is in the range of 0.05–3 at the line center, which are shown in cyan areas. The N_{H} for each $N_{\mathrm{H\,I}}$ are exhibited in gray contours.

report it in this paper. This paper is organized as follows. The data we used is described in Section 2. We analyze the absorption lines and estimate the corresponding ionic column densities in Section 3. We compare the observational results with photoionization models in Section 4 and discuss the results in Section 5. Our main findings are summarized in Section 6. Throughout this paper, we use a cosmology with $\Omega_m = 0.3$, $\Omega_\Lambda = 0.7$, and $H_0 = 70$ km s^{-1} Mpc^{-1}.

2. Observations and Data Reduction

J1220+4549 is a bright quasar at a redshift of $z = 3.275$ discovered by SDSS. The first spectrum was acquired with the SDSS spectrograph on 2004 March 26 (Abazajian et al. 2009). The spectrum spread over a wavelength range of $\lambda \sim 3800$–9200 Å in the observed frame. The second spectrum was taken using the Baryon Oscillation Spectroscopic Survey (BOSS) spectrograph (Dawson et al. 2013), which provided a more extended wavelength coverage at $\lambda \sim 3570$–10350 Å, on 2013 April 3. These two spectra share a similar spectra resolution of $R \sim 2000$. The SDSS broadband photometry was taken on 2003 March 24 (York et al. 2000). It is well consistent with the synthetic photometry data in the g, r, and i bands obtained from the SDSS and BOSS spectra (Abazajian et al. 2009; Dawson et al. 2013) as shown in Table 1. This indicates that there is little flux variations of this quasar over the time range of these observations. The Catalina Sky Survey[6]

[6] The Catalina Survey website site is at http://nesssi.cacr.caltech.edu/DataRelease/.

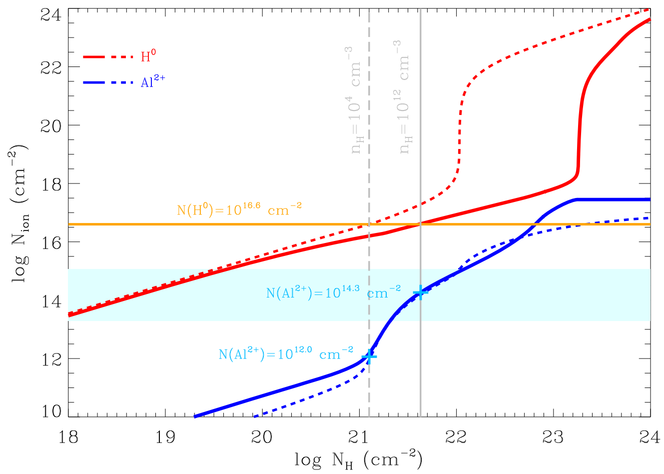

Figure 2. Photoionization models ($\log U = -1$) of low ($n_{\rm H} = 10^4$ cm^{-3}, dashed lines) and high density ($n_{\rm H} = 10^{12}$ cm^{-3}, solid lines). The $N_{\rm Al^{2+}}$ and $N_{\rm H^0}$ are shown as functions of $N_{\rm H}$. The light cyan area indicates the measurable $N_{\rm Al\,III}$ (see Section 1.1). $N_{\rm H^0}$ in the high-density model is lower than that in the low-density model since $N_{\rm H} \approx 10^{20}$ cm^{-2}. And the transfer from the H II zone to the H I zone occurs at $N_{\rm H}$, 1.3 dex smaller in the low-density model than in the high-density model. Therefore, at different densities, the same observed $N_{\rm H^0}$, e.g., $10^{16.6}$ cm^{-2}, implies very different $N_{\rm H}$ (as the solid and dashed gray lines exhibit), and subsequently very different $N_{\rm Al\,III}$ (as the two plus signs show).

performed an extensive photometric monitor (for 8 yr since 2005 June 10) for this object, and has 222 observations so far. The results show very weak long-term variability, no larger than 0.1 mag in the V band. Thus, we assume there is no evident time variances of the quasar, and we constructed a composite spectrum by combining the SDSS and BOSS spectra weighted according to their spectral S/Ns. We will use this spectrum for our further analysis. The spectrum is then corrected for Galactic extinction using the mean extinction curve (Fitzpatrick & Massa 2007), with selective extinction $E(B - V) = 0.012$ in the Galactic dust map (Schlegel et al. 1998). We transform the photometric data, the SDSS, BOSS, and the composite spectra into the rest frame with its emission redshift, as shown in Figure 3.

3. Spectral Analysis

3.1. Detected Absorption Lines

We identified the HiBAL troughs of C IV $\lambda\lambda$1548.20, 1550.77, Si IV $\lambda\lambda$1393.76, 1402.77 and N V $\lambda\lambda$1238.82, 1242.80, and the LoBAL troughs of Al III $\lambda\lambda$1854.72, 1862.79, C II λ1334.53, and Si III λ1206.50, as well as the Lyman series absorption troughs in the spectra of J1220+4549. In this section we will analyze the absorption lines in the spectrum of our source, deriving the column densities of the observed species. In the next section, these column densities will be used to derive the physical conditions in the absorbing gas.

3.2. Normalized Spectra

The pair-matching method is used to estimate the unabsorbed level of background flux, which is required for getting the normalized spectra of the abundant absorption lines and estimating the optical depth of each absorption line. A description of the philosophy and procedures can be found in Zhang et al. (2010) and Liu et al. (2015). Each individual BOSS spectrum from a library of non-BAL quasars was used to

Table 1
Photometric Data of SDSS J1220+4549

Band	Magnitude (mag)	Obs. Date (UT)	Facility
u	21.934 ± 0.169	2003 Mar 24	SDSS
g	18.886 ± 0.018	2003 Mar 24	SDSS
r	18.179 ± 0.050	2003 Mar 24	SDSS
i	17.771 ± 0.014	2003 Mar 24	SDSS
z	17.539 ± 0.022	2003 Mar 24	SDSS
g[a]	18.858 ± 0.115	2004 Mar 26	SDSS
r[a]	18.135 ± 0.062	2004 Mar 26	SDSS
i[a]	17.720 ± 0.022	2004 Mar 26	SDSS
g[b]	18.815 ± 0.434	2013 Apr 3	BOSS
r[b]	18.088 ± 0.134	2013 Apr 3	BOSS
i[b]	17.705 ± 0.063	2013 Apr 3	BOSS

Notes.
[a] Synthetic photometry data from SDSS spectrum.
[b] Synthetic photometry data from BOSS spectrum.

fit the spectral features of J1220+4549 surrounding BALs, with the absorption troughs being carefully masked out. A reduced χ^2 threshold (i.e., $\chi^2_{\rm reduced} < 1.5$) was often used to select the templates (Liu et al. 2015; Shi et al. 2016a). In addition, Tian et al. (2019) introduced a method to determine the most appropriate number of templates ($N_{\rm temp}$) to be used. First, the candidate templates are sorted by the reduced χ^2 in increasing order. We then constructed a composite template using the best $N_{\rm temp}$ templates. Thus, the standard deviation ($\sigma_{\rm nor}$) of the target spectrum divided by the composite template in absorption-free regions and the root mean square error (RMSE) of the composite template spectrum are estimated. We determine $N_{\rm temp}$ to be the value when $\sigma_{\rm nor} = \sigma_{\rm nor}(N_{\rm temp})$ is minimum. The median RMSE is less than ∼15% of the median error of the object spectrum. The details can be seen in Section 3.2 in Tian et al. (2019). The composite template is obtained by combining the selected individual candidate templates, each weighted according to their spectral S/N (the solid red lines in Figures 4(a1)–(a7)). The RMSE is much smaller than the error of the observed spectrum and is ignored in the rest of the analysis. After dividing the object spectrum by the composite template, the normalized spectra are obtained, as shown in the right panels of Figure 4.

In the left-hand panels of Figures 4(a1)−(a9) and the corresponding right-hand panels of Figures 4(b1)−(b9), we plot the spectral details of SDSS J1220+4549 around C IV λ1548.20, C IV λ1550.77, Si IV λ1393.76, Si IV λ1402.77, Al III λ1854.72, Al III λ 1862.79, C II* λ1335.70, C II λ 1334.53, and Si III λ1206.50, respectively. The C IV absorption trough, which is likely saturated, has a box-shaped bottom at a flux level of 1%–4% of the unabsorbed flux, indicating a nearly full coverage on the background source. The velocity range of the C IV trough is ∼2000 km s^{-1}, which agrees with the BAL definition (Weymann et al. 1991). The weight-averaged velocity of the absorption troughs, calculated from the Al III absorption trough, is −210 km s^{-1}.

3.3. Column Density Measurements

3.3.1. Al III

The Al III $\lambda\lambda$1854, 1862 absorption lines are well separated, as shown in Figure 4, benefited from the larger separation

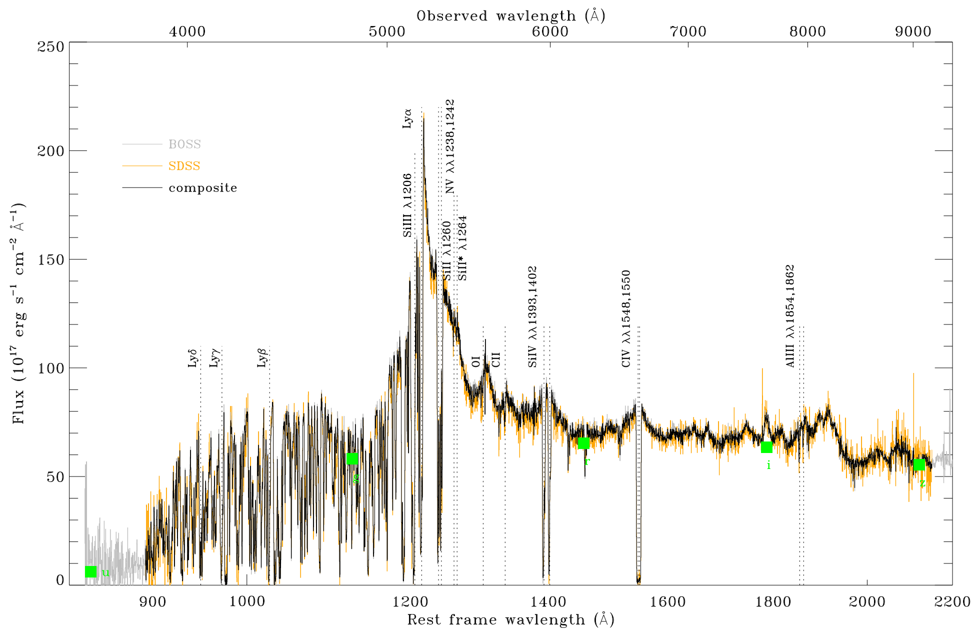

Figure 3. Rest-frame spectra of SDSS J1220+4549 from SDSS and BOSS. The green squares are the SDSS photometric data.

(1300 km s^{-1}) of these two lines. Theoretically, the optical depth (τ) is defined as (Savage & Sembach 1991)

$$I_r(v) = (1 - C_f(v)) + C_f(v)e^{-\tau(v)}, \quad (1)$$

where I_r is the normalized flux, and C_f is the covering factor. Using the covering factor ($C_f \sim 1$) suggested by the C IV absorption trough, the optical depth of Al III $\lambda\lambda$1854, 1862 can be calculated directly from the residual flux, I_r, in the normalized spectra according to $\tau = -\ln(I_r)$, which are shown in Figure 5. The ratio of the optical depths of the two Al III lines agree with the theoretical ratio of λf_{ik} (2: 1) within 1σ error. This reiterates that the Al III absorbing gas fully obscures the continuum source and the covering factor is close to 1.

Using the obtained optical depths, the column density of Al III is calculated according to Equation (2)

$$N_{\rm ion} = \frac{3.7679 \times 10^{14}}{f\lambda_0} \int \tau(v) dv \,({\rm cm}^{-2}). \quad (2)$$

The mean column density measured from the two lines is $(3.1 \pm 0.5) \times 10^{13}$ cm^{-2}.

It would be satisfactory to calculate the covering factor and the optical depth as a function of velocity. The data quality of the SDSS spectra (both of the moderate resolution and S/Ns), however, is not high enough for this calculation. We instead try to assess the effect of the covering fraction on the measurement of the Al III absorption lines, through the following exercise: we assume a uniform covering fraction, i.e., a covering factor C_f across the absorption trough that is independent of velocity. We think this is a reasonable assumption. In a recent study by Chen et al. (2021), a uniform coverage is assumed in the absorption-line analysis using the Keck/High Resolution Echelle Spectrometer and Very Large Telescope/UV-Visual Echelle Spectrograph spectra with $R \gtrsim 30{,}000$, much higher than that of SDSS data with $R \sim 2000$ used in this work. We let C_f vary from 0.2–1. The lower limit of C_f is chosen as the absorption depth of the Al III λ1854.72 trough. We calculated the reduced χ^2_ν between the spectrum of Al III λ1854.72 and Al III λ1862.79 for different C_f, and plot χ^2_ν as a function of C_f in the bottom panel in Figure 6. The column densities of Al III derived from Al III λ1854.72 and Al III λ1862.79 with different C_f are plotted in the top panel of this figure. The χ^2_ν reaches the minimum value of $\sim$0.8 when $C_f = 1$, and it increases monotonically as the C_f decreases. This suggests that the Al III absorption gas very likely has a full coverage of the background source, consistent with the adopted assumption. We also try to estimate 1σ, 2σ, and 3σ confidence intervals of C_f (shown as gray, cyan, and green plus signs). For example, $N_{\rm Al\,III}$ is $\sim 6 \times 10^{13}$ cm^{-2} when the C_f is at the 1σ level ($C_f \sim 0.67$), which is nearly two times that when assuming $C_f = 1$. Al III absorption gas does not necessarily have the same covering fraction as that of C IV. If it indeed had a partial coverage, the Al III column density we measured should be taken as a lower limit. The true $N_{\rm Al\,III}$ might be larger than the value given here, and we would expect an even higher $n_{\rm H}$, as predicted in Figure 1.

3.3.2. C II

The C II absorption trough is a blend of C II λ1334.53 and C II* λ1335.70, which are separated from each other by only 263 km s^{-1} (e.g., Borguet et al. 2012a). The two transitions are from different lower levels. And the ratio of column densities on the two lower levels, $N_{\rm C\,II}/N_{\rm C\,II*}$, is dependent on the electron density ($n_{\rm e}$). Since $n_{\rm e} \approx 1.2\, n_{\rm H}$, the ratio would also be a function of $n_{\rm H}$. Theoretical simulations (Tian et al. 2019) predict that the ratio of the two lines is $\sim$0.5:1 when $n_{\rm H}$ is well above the critical density ($\sim 2.8 \times 10^3$ cm^{-3}, Meijerink et al. 2007) and is increased to $\sim$2.8:1 when $n_{\rm H} = 10$ cm^{-3}. Thus, the optical depth ratio of C II λ1334.53 to C II* λ1335.70 would also vary from $\sim$2.8:1 at $n_{\rm H} = 10$ cm^{-3} to $\sim$0.5:1 at higher densities. In order to measure the column density of C II, we shift the Si IV λ1402.77 absorption profile to C II λ1334.53 and C II* λ1335.70 wavelengths, and use the profile as a template to fit the C II absorption trough, applying a different optical depth ratio value for different $n_{\rm H}$. The best-fit column density of C II λ1334.53 is $N_{\rm C\,II} = (5.0 \pm 2.6) \times 10^{13}$ cm^{-2} with $n_{\rm H} \gtrsim 2.8 \times 10^3$ cm^{-3} (low-density probability, $n_{\rm H} < 10$ cm^{-3}, can be rejected at the 3σ level).

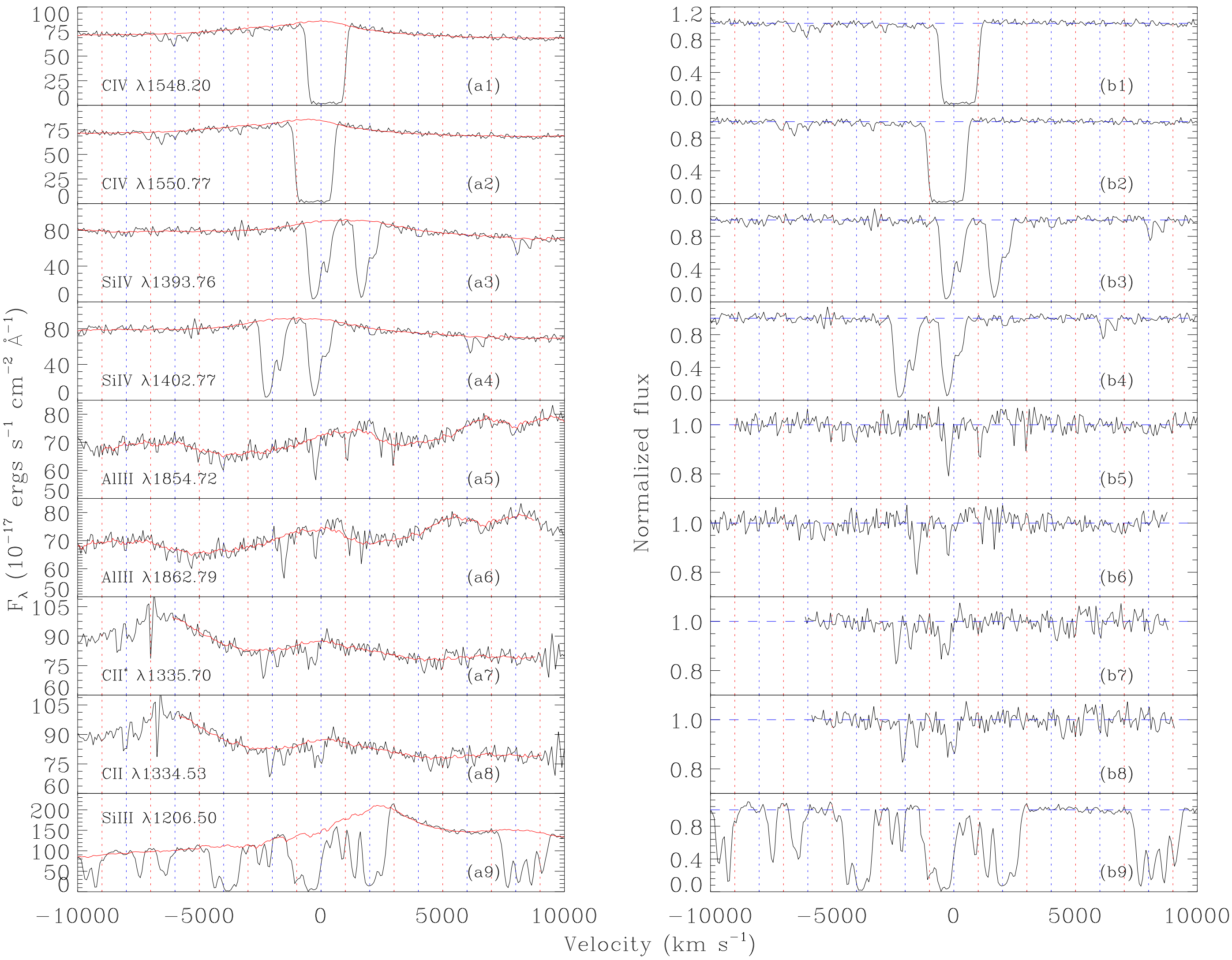

Figure 4. Left: the velocity structure in the C IV, Si IV, Al III, C II, and Si III regions with respect to C IV λ1548.20, C IV λ1550.77, Si IV λ1393.76, Si IV λ1402.77, Al III λ1854.72, Al III λ1862.79, C II* λ1335.70, C II λ1334.53, and Si III λ1206.50. The mean template spectra by the pair-matching method are exhibited in solid red lines. Right: the normalized spectra corresponding to the left panels.

3.3.3. Si IV Lower Limits

When inspecting Figures 4(b3)–(b4), it is clear that the BAL troughs of Si IV $\lambda\lambda$1393.76, 1402.77 are well detached. We estimated the optical depth of the two absorption lines using Equations (1), and found that the ratio of the optical depth of the two lines is significantly larger than 2, which is the ratio of λf_{ik} of the two lines. Therefore, Si IV might be saturated. Using Equation (2), we then directly estimated the column density of $\mathrm{Si}^{3+}_{\mathrm{ground}}$ by Si IV λ1393.76 and Si IV λ1402.77, respectively. The values are $(8.4 \pm 0.07) \times 10^{14}\,\mathrm{cm}^{-2}$ and $(1.3 \pm 0.07) \times 10^{15}\,\mathrm{cm}^{-2}$, and the latter should be treated as a more tight lower limit of the Si IV column density.

3.3.4. Neutral Hydrogen

To estimate the neutral hydrogen column density for the absorber in J1220+4549, the absorption-free spectrum in the Lyman series wavelength region should be determined first. In the Lyα region, the pair-matching method (see Section 3.2 for details) was used to construct the absorption-free template. For the wavelength regions shorter than the Lyα region, we modify the composite spectrum of Zheng et al. (1997) to roughly match the absorption-free level in the Lyβ region and blueward of it. The composite spectrum is multiplied by a one-order polynomial to take into account of the possible reddening and flux calibration problems. Then we reconstruct the absorption-free spectrum by stitching the two parts together, shown as the orange line in Figure 7(a). The corresponding normalized spectrum are plotted in Figure 7(b) and the absorption line details of Lyα, Lyβ, Lyγ, Lyδ, and Lyϵ are presented in Figures 7(c)–(g).

Assuming the velocity structures of the Lyman series absorption troughs are the same as that of Si IV, we estimate the neutral hydrogen column density by shifting the Si IV λ1402.77 absorption profile to the Lyman series wavelength region and use the profile as a template to match these absorption lines. The relative optical depth values τ_i of Lyman series absorption lines are determined by the known oscillator strengths.[7] It is found that the center and blue side of Lyδ, as well as the center and red side of the Lyϵ absorption lines, can

[7] $\tau_i = R\tau_{\mathrm{Ly}\alpha}$, where $R = f_i\lambda_i/f_{\mathrm{Ly}\alpha}/\lambda_{\mathrm{Ly}\alpha}$ is the ratio of the optical depth of Lyman series to that of Lyα, the f_i are the oscillator strengths, and the λ_i are the wavelengths of the lines.

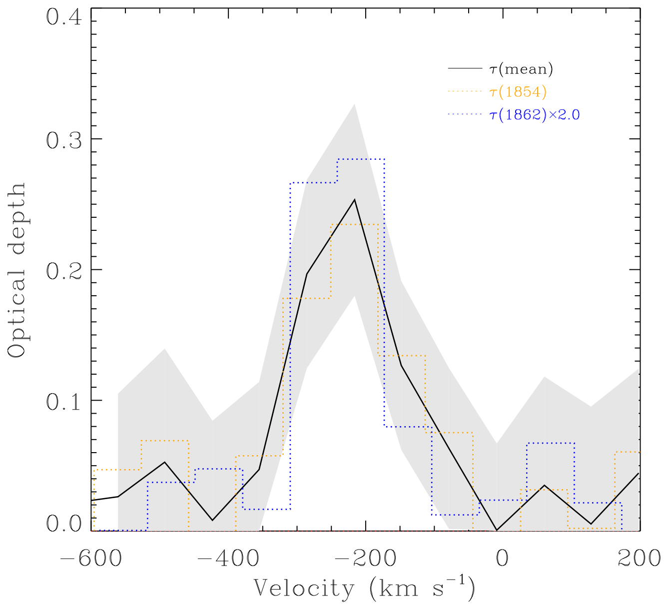

Figure 5. Optical depth of the Al III absorption line assuming full coverage. The ratio of λf_{ik} for Al III λ1854 to Al III λ1862 is 2.0. We find that, after multiplying the corresponding ratio, the apparent optical depth of Al III λ1682 matches that of Al III λ1854 within 1σ error (shown in gray).

be well reproduced when the neutral hydrogen column density reaches $\sim 4.0 \times 10^{16}\,\mathrm{cm}^{-2}$. The best fit corresponds to a chi-square denoted as χ_0^2. We then calculated the upper and lower limits of $N_{\mathrm{H\,I}}$ when the chi squares are $\chi_0^2 \pm 1$, and the results are listed in Table 2. As shown in Figure 7(b) (the details are presented in Figures 7(f) and (g) for Lyδ and Lyϵ), the simulations mismatch the red side of Lyδ and the blue side of the Lyϵ absorption troughs, which might be due to contamination from intervening Lyman series absorption lines (e.g., Lynds 1971; Weymann et al. 1981). There are also remarkable residual fluxes for the Lyα and Lyβ absorption troughs, and the origin of them will be discussed in Section 5.3.The estimated ion column densities are summarized in Table 2.

The Lyman series absorption troughs might be contaminated by the Lyα forest. The number density of the Lyα forest is $dN/dz = 3.5(1+z)^{2.7}$ in the redshift range of [2.1, 3.5] (Kim et al. 1997). We use Lyδ absorption as an example, which is at $\sim$950 Å in the quasar's rest-frame spectrum ($\sim$4061 Å in observed frame), with a width of about 1000 $\mathrm{km\,s^{-1}}$, corresponding to a $\delta z = 0.014$. Thus, we are likely to have one Lyα forest absorption line around the Lyδ absorption trough. Since typical forest absorbers have $\log N_{\mathrm{H\,I}}$ of [14–17.2] cm^{-2} and a broadening width b of 20–40 $\mathrm{km\,s^{-1}}$ (Kim et al. 1997). We then generate the Lyα absorption line using $\log N_{\mathrm{H\,I}} = 17.2\,\mathrm{cm}^{-2}$ and $b = 40\,\mathrm{km\,s^{-1}}$ with the typical resolution of SDSS spectrum. Since the b value of the Lyα forest system is very low, the modeled absorptions are quite weak as compared with the observed Lyδ absorptions. The contribution to observed $N_{\mathrm{H\,I}}$ should be less then $\sim$22%, which can be neglected. The contribution is only $\sim$6% in the case of the Lyα forest with $\log N_{\mathrm{H\,I}} = 14\,\mathrm{cm}^{-2}$ and the same b value. In addition, the contamination from potential Lyα forest absorptions will lead to an overestimation of H I column density, which will in turn also favor a larger n_{H} as predicted by photoionization simulations (see Figure 1).

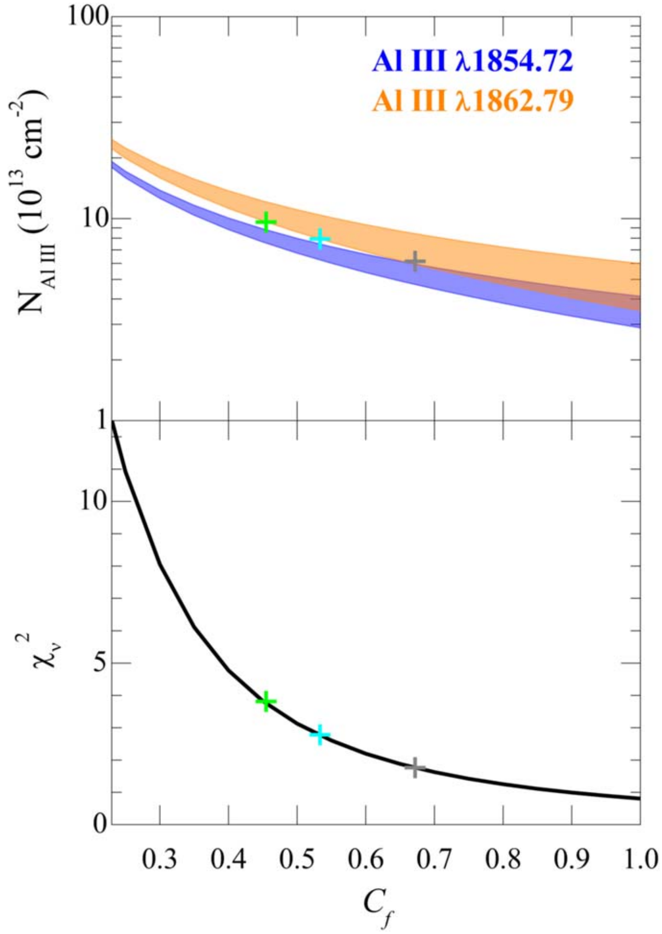

Figure 6. Top: the column densities of Al III, derived from Al III λ1854.72 and Al III λ1862.79 with 1σ errors, are shown as a function of C_f. Bottom: the reduced χ_ν^2 between Al III λ1854.72 and Al III λ1862.79 are exhibited as a function of C_f. The 1σ, 2σ, and 3σ confidence intervals of C_f and $N_{\mathrm{Al\,III}}$ are indicated by the gray, cyan, and green plus signs, respectively.

3.3.5. Si III Lower Limit

Figures 3 and 4 show that the Si III absorption line might be heavily saturated. We estimate the lower limit of Si III column density by shifting the Si IV λ1402.77 absorption profile to the Si III wavelength region. Then the template was used, with Equation (2), to calculate the column density lower limit of $\mathrm{Si}^{2+}_{\mathrm{ground}}$, and the result was listed in Table 2.

3.4. Other Estimated Properties of J1220+4549

With the existing data at hand, we can also estimate the BH mass and the accretion rate of this quasar. We used the method reported by Vestergaard & Peterson (2006, their Equation (7)), which is based on the FWHM (C IV) and λL_λ(1350 Å), to estimate the mass of the central BH. The λL_λ luminosity is corrected for the broadband extinction using the LMC extinction curve. The FWHM(C IV) is 5217 $\mathrm{km\,s^{-1}}$, estimated from the rebuilt C IV emission line by the pair-matching method (see Section 3.2). Thus, the central BH mass is estimated to be $6.7 \times 10^9 M_\odot$. Then, we calculated the bolometric luminosity using the conversion by Runnoe et al. (2012, their Equations (9) and (13)), which is based on λL_λ(1450 Å), giving $L_{\mathrm{bol}} \approx 4.27 \times 10^{47}\,\mathrm{erg\,s^{-1}}$. The corresponding Eddington luminosity is $1.01 \times 10^{48}\,\mathrm{erg\,s^{-1}}$, and the Eddington ratio is $L_{\mathrm{bol}}/L_{\mathrm{Edd}} \sim 0.42$. The accretion rate of the

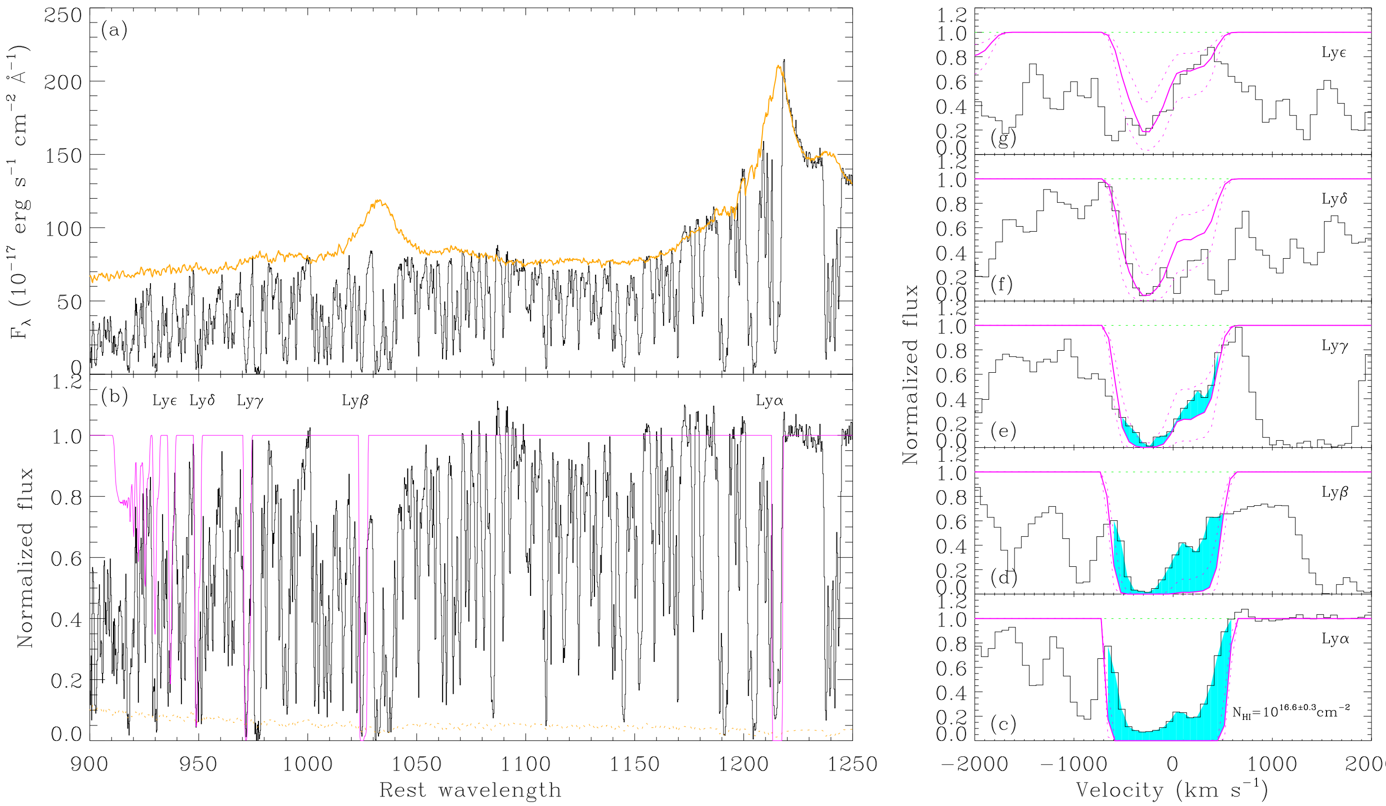

Figure 7. Comparisons between the observed Lyman series troughs and that of the predicted results, assuming that the velocity structure of the Lyman series absorption troughs are the same as that of Si IV λ1402.77. The fluxes of the Lyman absorption lines (magenta) predicted with $N_{\rm H\,I} = 4 \times 10^{16}$ cm^{-2} agree well with observed results. This result is also changed by $\pm$0.3 dex, and the corresponding absorption fluxes are plotted in magenta dashed lines. They clearly show deviations from the observations. Thus, we approximately considered the $\pm$0.3 dex as the upper limit of the errors. The residual flux in the line center is labeled in cyan.

Table 2
Estimated Column Densities of the Absorber in SDSS J1220+4549

Ion	$N_{\rm ion}$ (cm^{-2})
Si IV	$>1.3 \times 10^{15}$
Si III	$>2.3 \times 10^{14}$
C II	$(5.0 \pm 2.6) \times 10^{13}$
Al III	$(3.1 \pm 0.5) \times 10^{13}$
H I	$4.0^{+0.9}_{-1.0} \times 10^{16}$

central BH, based on the bolometric luminosity, is

$$\dot{M}_{\rm acc} = \frac{L_{\rm bol}}{\eta c^2} = 75.2\ M_\odot\ {\rm yr}^{-1}, \tag{3}$$

where we assumed an accretion efficiency η of 0.1, and c is the speed of light.

4. Physical Properties of the Absorber

4.1. Building Photoionization Models

Armed with the column density measurements of the H I, C II, and Al III and the lower-limit results of Si IV and Si III, we can proceed to use them to constrain the properties of the absorber. The most key parameters characterizing the physical conditions of the absorber are $N_{\rm H}$, $n_{\rm H}$, and U. The other parameters, such as the distance to the central BH ($r_{\rm abs}$), mass-flow rate ($\dot{M}_{\rm out}$) and kinetic luminosity ($\dot{E}_k$), can be obtained accordingly (e.g., Borguet et al. 2012a).

We use the Cloudy (c17; Ferland et al. 1998, 2017) model to estimate the three parameters. We assume a slab-shaped geometry, a uniform density, a homogeneous chemical composition (solar values), and no dust from the medium (Shi et al. 2016a, 2016b). The incident SED applied is a combination of the *big bump* component and a power-law X-ray component spanning 13.6 eV $-$100 keV (formalized as $\nu^{\alpha_{\rm UV}} \exp^{(-h\nu/kT_{\rm BB})} \exp^{(-kT_{\rm IR}/h\nu)}$ and $\alpha\nu^{\alpha_X}$ in Cloudy, respectively), as observed in a typical AGN. These parameters are chosen to ensure the big bump peaked at 1 Ryd, the optical to UV slope, $\alpha_{\rm UV}$, to be -0.5 (Elvis et al. 1994), and the X-ray to UV slope to be 1.4 (Zamorani et al. 1981), and lastly, the slope of the X-ray component, α_X, is -1 (Elvis et al. 1994).

However, exploring the best model that can simultaneously reproduce the observed column densities of several ions, in the 3D parameter space ($N_{\rm H}$, $n_{\rm H}$, and U), is challenging. Thus, we use the observed H I column density to reduce the number of free parameters by 1. We will keep the $n_{\rm H}$ and U free, and for each set of $n_{\rm H}$ and U values, $N_{\rm H}$ can be determined from the observed H I column density.

Adopting the solar abundance, we run the simulations over $-4 \leqslant \log U \leqslant 4$, $0 \leqslant \log n_{\rm H}$ (cm^{-3}) $\leqslant 15$. For a given $n_{\rm H}$ and U, we find the $N_{\rm H}$ value where the predicted H I column density matches the observed one. In the end, the relations between $N_{\rm H}$ and (U and $n_{\rm H}$) can be built,

$$N_{\rm H} = f(U, n_{\rm H}). \tag{4}$$

We plot the $N_{\rm H}$ contours as a function of $\log U$ and $\log n_{\rm H}$ in Figure 8.

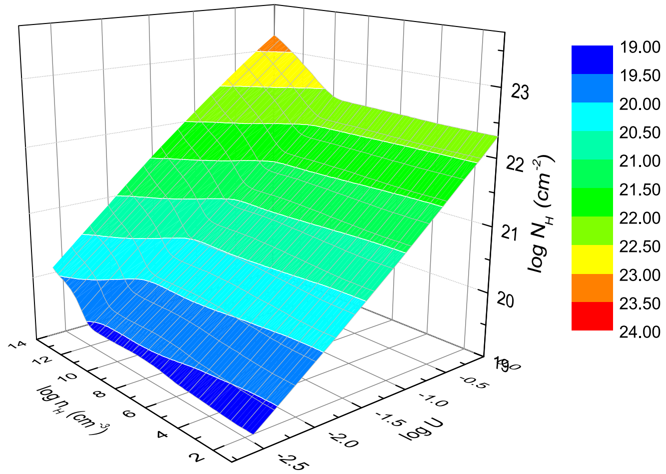

Figure 8. The $N_{\rm H}$ as a function of $n_{\rm H}$ and U in the condition when the modeled H I column density reaches the observed value. Therefore, the best model (U, $n_{\rm H}$, and $N_{\rm H}$) should appear in the surface.

4.2. Ionization, Density, and Column Density

For a set value of (U and $n_{\rm H}$), $N_{\rm H}$ can be determined via the H I column density (Figure 8). With these three values, we can use the model to estimate the absorption strengths of various metal ions, which can be compared with the observed absorption lines. In Figure 9, we show what would be the parameter spaces in (U and $n_{\rm H}$) that different observed ionic column densities allow or do not allow. First, the areas marked by gray are excluded by the lower limits of the Si IV and Si III column densities. The parameter spaces suggested by the measured column densities of C II and Al III are shown as the red and blue regions, respectively. The best model is the intersection of these two areas, marked as the open square. It gives the best-estimated log $N_{\rm H}$, log U, and log $n_{\rm H}$ to be $21.0 \pm 0.3\ {\rm cm}^{-2}$, -1.25 ± 0.40, and $11.03 \pm 0.35\ {\rm cm}^{-3}$.[8] It is clear that the best model agrees with the lower limits given by the $N_{\rm Si\ IV}$ and $N_{\rm Si\ III}$. The Si IV column density, suggested by the best model is $\sim 3.0 \times 10^{15}\ {\rm cm}^{-2}$, only slightly larger than the observed lower-limit value listed in Table 2. We note that the estimated density of absorbing gas from the best model is very high. This is well within the regime of densities of the BLR gas. We discuss this further in Section 5.

The errors of the three parameters propagated from the error of $N_{\rm H\ I}$ are considered as follows. Two figures similar to Figure 9 are drawn, using the upper and lower limits of $N_{\rm H\ I}$ as listed in Table 2, to derive the corresponding gas densities, which are treated as the lower and upper limits of $n_{\rm H}$. Thus, the $n_{\rm H}$ error is about ± 0.5 dex. Meanwhile, the errors of U and $N_{\rm H}$ contributed from the error of $N_{\rm H\ I}$ are very small.

We also try to find out how the best model depends on the metallicity of the simulated gas. We consider four other metallicities, 2.0, 3.0, 5.0, and $10.0\,Z_\odot$, respectively. We found that in the case of $2.0\,Z_\odot$, as shown in the $2.0\,Z_\odot$ panel in Figure 10, the best model is very similar to that of $1.0\,Z_\odot$. In the case of $3.0\,Z_\odot$, high density was also obtained, log $n_{\rm H} \sim 10\ {\rm cm}^{-3}$, with similar U and $N_{\rm H}$ to that of 1.0 and $2.0\,Z_\odot$. In the case of 5.0 and $10.0\,Z_\odot$, it is clear that there are no set of parameters which

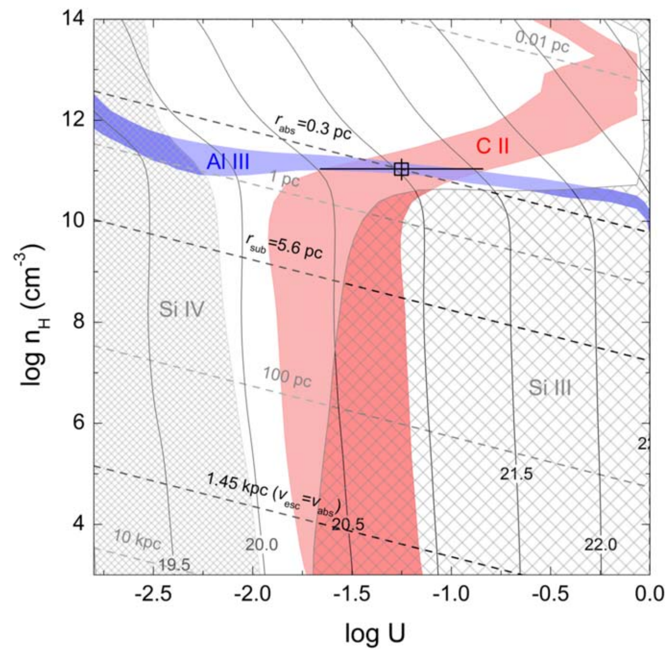

Figure 9. Photoionization models of the absorber in SDSS J1220+4549 assuming a metallicity of $1.0\,Z_\odot$. First, The areas marked by dense and sparse gray crossing lines are excluded by the lower limit of the Si IV and Si III column densities. The blue and red shaded regions represent the parameter space in ($N_{\rm H}$, U, and $n_{\rm H}$) allowed by the observed $N_{\rm Al\ III}$ and $N_{\rm C\ II}$ (with 1σ error). The black solid lines represent $N_{\rm H}$ as a function of U and $n_{\rm H}$, see Equation (4), in the condition when the modeled column density of H I reaches the observed value. The best model is marked by an open square. The errors of U and $n_{\rm H}$ are approximately estimated by the difference between the edge values of the intersection and the best model (open square) in the log U and log $n_{\rm H}$ directions. Then, the $N_{\rm H}$ error is estimated accordingly by Equation (4).

could predict the measured Al III and C II column densities simultaneously, as shown in the 5.0 and $10.0\,Z_\odot$ panels in Figure 10. Therefore, we suppose that the metallicity might be lower than $5\,Z_\odot$. A similar upper limit of metallicity was also found by Lu et al. (2008), who reported that the gas metallicity is likely no higher than $4\,Z_\odot$.

For quasars of similar redshift as our object, the properties of the absorbing gas can be probed via the P V $\lambda\lambda$1117.98, 1128.01 absorption lines, located in the far-UV wavelength region (e.g., Hamann 1998), as these two lines are usually not blended. However, they are heavily contaminated by the Lyα forests, which makes accurate measurements difficult.

The P V $\lambda\lambda$1118.98, 1128.01 absorption doublets are also covered by SDSS/BOSS observations, but they are embedded in the Lyα forest, and we have to make certain assumptions regarding their profiles to measure their absorption strengths. The P V column density predicted by our best model is $\sim 6.1 \times 10^{13}\ {\rm cm}^{-2}$. We simulated the absorption troughs of these two lines using the best model, assuming their absorption profiles are the same as that of Si IV λ1402.77, as the blue and red lines show in the top panel in Figure 11. We also simulated the S IV λ1062.66 and S IV* λ1073.02[9] absorption troughs using the same methods as used for P V, as shown in the bottom panel in Figure 11. The depths of simulated absorption troughs, especially for P V λ1118.98 and S IV λ1062.66, are shallower than the corresponding observations. This is reasonable, considering that there are non-negligible contaminations from

---

8 As shown in Section 3.3.1, Al III is probably close to full coverage. The $N_{\rm Al\ III}$ is $\sim 6 \times 10^{13}\ {\rm cm}^{-2}$ when C_f is at the 1σ level ($C_f = 0.67$, see Figure 6), which is about two times of that when assuming $C_f = 1$. We calculated the corresponding $n_{\rm H}$ with this $N_{\rm Al\ III}$, and the value is about 0.3 dex higher than that when assuming $C_f = 1$.

9 It is blended of S IV* λ1072.973 and S IV* λ1073.518 with the optical depth of 0.042 and 0.0039.

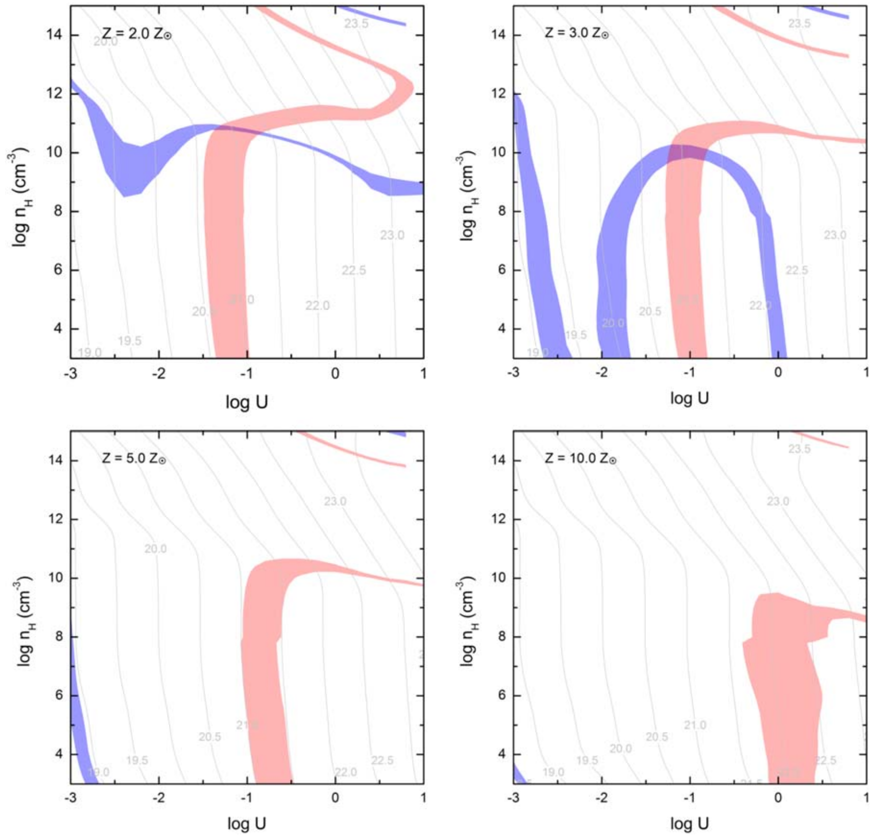

Figure 10. Photoionization models of the absorber in SDSS J1220+4549 assuming a metallicity of 2.0, 3.0, 5.0, and 10.0 $Z_{\odot}$, respectively. The blue and red shaded regions represent the locus of points ($N_{\rm H}$, U, and $n_{\rm H}$) able to reproduce the observed $N_{\rm Al\,III}$ and $N_{\rm C\,II}$ (with 1σ error). The gray lines are $N_{\rm H}$ as a function of U and $n_{\rm H}$, see Equation (4), in the condition when the modeled column density of H I reaches the observed value.

the absorption troughs of the Lyman series. In addition, we noticed that J1200+4549 showed no Si II λ1260 and Si II* λ1264 absorptions. The predicted column densities with our best model of Si II and Si II* are 1.55×10^{12} and $3.04 \times 10^{12}\,{\rm cm}^{-2}$, which is hard to observe with the present S/N. These observations are all in agreement with the solution we obtained as shown in Figure 9.

5. Discussions

5.1. Diagnosis of High-density Gas via the BALs

As shown in previous sections, we demonstrated that by combining the H I column density and the Al III column density, it can be powerful to identify the high-density absorbing gas, in a way that if the Al III absorption line can be detected in the condition of $15.4 \lesssim \log N_{\rm H\,I}\,({\rm cm}^{-2}) \lesssim 16.5$, the absorber should be in high dense ($n_{\rm H} > 10^{10}\,{\rm cm}^{-3}$) regions. For our quasar, the observed H I column density is around $\log N_{\rm H\,I}\,({\rm cm}^{-2}) \sim 16.6$, and the best-fit $\log n_{\rm H}$ is $11.03 \pm 0.50\,{\rm cm}^{-3}$.

Previously, the estimation of the densities of the absorbing gas usually relied on detecting the excited states of singly or multiply ionized absorption lines, such as Si II* λ1264.73, C II* λ1335.70, N III* λ991.57, S III* λ1015.63, S IV* λ1072.97, Fe II, etc. The ratios of these excited states absorbing lines to their ground-state counterparts are sensitive to the densities. The detection of these excited-state ion lines, however, often requires spectra of high resolution. They are also not always available for quasars at various redshifts. In addition, absorbing gas probed via these lines are often of much lower density (e.g., Borguet et al. 2012a; Chamberlain & Arav 2015; Ji et al. 2015; Xu et al. 2018, 2019), for the reasons we lay out below. In this aspect, the method mentioned in this paper is complementary to these previously used methods in measuring gas densities.

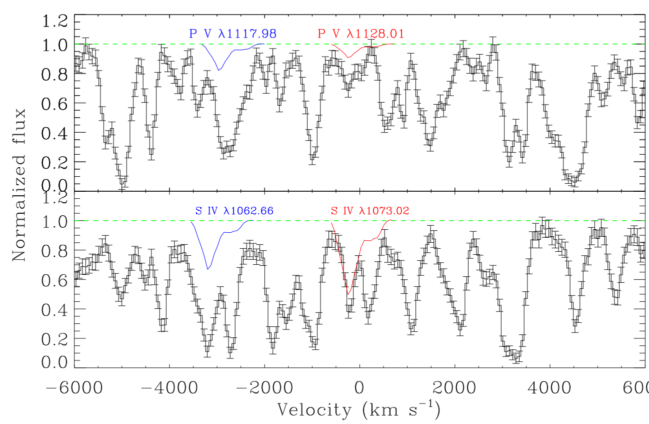

Figure 11. P V $\lambda\lambda$1117.98, 1128.01 and S IV λ1062.66 and S IV* λ1073.02 absorption troughs. These four absorption troughs, simulated by Si IV λ1402.77 with the best model in Figure 9, are shown as blue and red lines.

It is helpful to compare our results with these previous studies to understand why they often obtain low-density solutions for the absorbing gas of their objects, while we get the high-density solution for J1220+4549. Our result suggests that if the $N_{\rm H\,I}$ of the absorber is measured to be relatively low at $15.4 \lesssim \log N_{\rm H\,I}\,({\rm cm}^{-2}) \lesssim 16.5$, and if the Al III absorption line doublet can be detected, the absorbing gas can be diagnosed as high density. As can be seen, there are two conditions for the diagnosis to work: a measured relatively low

$N_{\rm H\,I}$ and a detection of the Al III absorption line. First, the Al III wavelength region was not covered in the spectrum in Borguet et al. (2012a), where they reported the $n_{\rm H}$ of two trough systems (T2) and (T3) ($\log\ n_{\rm H} < 10^2\ {\rm cm}^{-3}$). Although the observed log $N_{\rm H\,I}$ ([15.97, 16.19] for T2, 15.63 for T3) are in our suggested range, the simulated log $N_{\rm Al\,III}$ using our model with the reported parameters are too small (12.63 and 11.96 $\rm cm^{-2}$ for T2 and T3) to be detected, thus the small $n_{\rm H}$ (Borguet et al. 2012a) does not contradict our work (see Figure 1). Second, Al III absorption troughs were detected in six sources in previous works with observed $n_{\rm H} \lesssim 10^4\ {\rm cm}^{-4}$ (Borguet et al. 2012b; Chamberlain & Arav 2015; Xu et al. 2018, 2019); however, the reported $N_{\rm H\,I}$ are are all lower limits and the predicted value using our model with the reported parameters are all larger than $10^{17}\ {\rm cm}^{-3}$, which are greater than our suggested range. Third, the reported $n_{\rm H}$ in J1135+1615 are lower limit ($\log n_{\rm H} > 5.4\ {\rm cm}^{-3}$) (Xu et al. 2019). The log $N_{\rm H\,I}$ we predicted is $\log\ N_{\rm H\,I} < 17.30\ {\rm cm}^{-2}$. We found that the predicted $N_{\rm H\,I}$ is smaller with larger $n_{\rm H}$. The predicted log $N_{\rm H\,I}$ is 16.7 $\rm cm^{-2}$ when log $n_{\rm H}$ is 11.0 $\rm cm^{-3}$, which is very similar to our source. In conclusion, these previously reported results do not contradict our conclusions.

With the density of the absorbing gas measured, we can estimate the distance ($r_{\rm abs}$) of the absorber away from the central source. We use the definition of the ionization parameter U,

$$U = \frac{Q_{\rm H}}{4\pi r^2 n_{\rm H} c}, \qquad (5)$$

where $Q_{\rm H}$ is the total rate of hydrogen-ionizing photons emitted by the central source (e.g., Dunn et al. 2010). $Q_{\rm H}$ equals $L(<912)/\overline{E_{\rm ph}(<912)}$, where $L(<912)$ is the ionizing luminosity of the continuum source, and $\overline{E_{\rm ph}(<912)}$ is the average energy for all ionizing photons. Thus, $Q_{\rm H}$ can be obtained when the luminosity and the SED shape of the central engine are known. Applying the observed continuum flux in the SDSS rest-UV spectrum and the AGN SED used in the simulation, we determine the distance of the absorber as being $r_{\rm abs} = 0.3^{+0.23}_{-0.13}$ pc for our best model. This distance is very close to the central BH. We discuss the origin of this absorber in the next subsection.

5.2. Origin of the Absorber

5.2.1. From Dusty Torus

We first ask if the absorbing gas could be from the torus region. The inner radius of the dusty torus is often approximated as the sublimation radius, $R_{\rm sub} = 1.3 L_{\rm UV,46}^{1/2} T_{1500}^{-2.8}$ pc (Barvainis 1987), where $L_{\rm UV,46}$ is the UV luminosity in units of $10^{46}\ {\rm erg\ s}^{-1}$ estimated using $\lambda L_\lambda(1350\ \text{Å})$, and T_{1500} is the grain evaporation temperature in units of 1500 K, which is ∼1. With these information, we estimate the sublimation radius for our source to be $R_{\rm sub} \sim 5.6$ pc. This is more than one order of magnitude larger than the absorber distance $r_{\rm abs}$ we determined above (see Section 5.1). Kishimoto et al. (2007), when comparing $R_{\rm sub}$ with the results of RMs, suggested that the inner radius of a dusty torus obtained in this way can be overestimated by a factor of approximately 3. However, even when we take into account this factor of 3, $R_{\rm sub}$ is still significantly larger than $r_{\rm abs}$. Thus, it suggests that the absorbing gas of J1220+4549 might not rise from a dusty torus outside of the dust sublimation radius.

5.2.2. From the BLR

As mentioned before, the density of the absorbing gas and its distance to the central BH are both estimated to be close to the BLR. Could the absorbing gas actually come from the BLR? We first use the results from the RM (for reviews, see Peterson 1993) to estimate the size scale of the BLR of our source and make comparisons. Two of the main results of RM campaigns are that high-ionization ions reside at smaller distances from the accretion disk than low-ionization ions (Clavel et al. 1991) and that for the emission line from different AGNs, the $R_{\rm BLR}$ is roughly positively correlated with the square root of AGN luminosity (Kaspi et al. 2005).

Bentz et al. (2009) analyzed a sample of AGNs with a wide luminosity range and gave a relationship between the $\rm H_\beta$ BLR size and the quasar UV luminosity of

$$\log(R_{\rm BLR}) = -21.0 \pm 1.8 + (0.511 \pm 0.041)\log(\lambda L_\lambda(5100\ \text{Å})). \qquad (6)$$

Assuming that J1220+4549 has a similar spectral shape as typical quasars from the SDSS quasar sample (Vanden Berk et al. 2001), then $\lambda L_\lambda(1350\ \text{Å})$ is about twice $\lambda L_\lambda(5100\ \text{Å})$. $\lambda L_\lambda(1350\ \text{Å})$ of $1.86 \times 10^{47}\ {\rm erg\ s}^{-1}$ gives $\lambda L_\lambda(5100\ \text{Å}) = 9.3 \times 10^{46}\ {\rm erg\ s}^{-1}$ and $R_{\rm BLR} = 1002$ lt-days $= 0.84$ pc.

We also use the C IV radius–luminosity relation given by Lira et al. (2018, their Equation (1)), which is updated from Kaspi et al. (2007) but incorporates 11 high-redshift, high-luminosity quasars. They gave an empirical relation between the C IV BLR size and the quasar UV luminosity

$$\frac{R_{\rm C\,IV}}{10\ \text{lt-days}} = (0.22 \pm 0.10)\left[\frac{\lambda L_\lambda(1345\ \text{Å})}{10^{43}\ {\rm erg\ s^{-1}}}\right]^{(0.46\pm0.08)}. \qquad (7)$$

For J1220+4549, the estimated $R_{\rm BLR}$ is ≈ 202 lt-days = 0.17 pc.

Since C IV is of higher excitation than Hβ, it is expected that the C IV BLR locates closer to the central BH than that of Hβ (e.g., Clavel et al. 1991). The estimated location of the absorber of our quasar (see Section 5.1 for details) lies in between C IV and Hβ $R_{\rm BLR}$, and agree well with the idea that the absorbing gas of J1220+4549 might be from the BLR. Adopting the above parameters derived from the absorption lines, we export the expected line intensity ratio of C IV/Hβ, and found this ratio is 15 times larger than the averaged value of SDSS quasars (Vanden Berk et al. 2001). This indicates that the absorber might be closer to the C IV high-ionization emission line region, which consists with the above distance estimates.

This absorbing BLR gas might have an origin from further within. It is suggested that some of the outflowing wind originated from the accretion disk may not gain enough acceleration (e.g., Risaliti & Elvis 2010) and can get accumulated at the BLR regions (e.g., Różańska et al. 2014) to form the absorbing gas in the BLR. The properties of our quasar also agree with this picture. It is well known that the escape velocity of the outflowing medium is $v_{\rm esc} = \sqrt{2GM_{\rm BH}/r}$, where G, $M_{\rm BH}$, and r are the gravitational constant, BH mass, and distance to the central BH, respectively. For J1220+4549, the $v_{\rm esc}$ at a distance of $r = 0.3$ pc, where the absorber is estimated to be located at, is ∼13,849 km $\rm s^{-1}$. This is much larger than the radial velocity ($v_{\rm abs} \sim 200$ km $\rm s^{-1}$) measured from the blueshifted absorption lines. Thus, it is very likely that the absorber in our source cannot escape from the gravitational field of the central BH. In fact, with such a small $v_{\rm abs}$, only when the absorber is located at a galactic scale, as far as

1.45 kpc ($v_{esc} = v_{abs}$, as shown in Figure 9), can the absorber have the chance to escape from the gravitational field of the central BH. Or when the central BH mass is less than $6.0 \times 10^6 M_\odot$, an absorber can escape at 0.3 pc with ∼200 km s^{-1}. This is three orders of magnitude smaller than that of J1220+4549 (see Section 3.4). This suggests that the absorber might be the failed disk wind, which can be observed if they happen to locate on the line of sight, as predicted by simulations (Risaliti & Elvis 2010; Quera-Bofarull et al. 2020). The simulations of Różańska et al. (2014) show that the disk wind from the outermost accretion disk atmosphere can build up a dense absorber ($n_H = 10^{10}$–10^{12} cm^{-3}), with a location of 0.1 pc, which is similar to that of our source.

5.3. Origin of the Residual Lyα

Significant residual flux upon the Lyα (Figure 7(c)) and Lyβ (Figure 7(d)) absorption troughs were detected, and weak residual flux was also seen on the Lyγ (Figure 7(e)) absorption trough. The absorbing gas is radiated from the center ionizing source. At the same time, it should produce emission lines through photoionization processes. The residues in the absorbing lines can be naturally interpreted as the emission from absorbing gas. Adopting the above parameters derived from the absorption lines, we use the Cloudy code to export the expected emission line intensities and compare them with the absorbing lines residues measured in this object. We found that the model expected Lyα intensity is about twice C IV, while the observed Lyα residue is much larger than the C IV residue. A possible explanation is that a large fraction of the Lyα residue is contributed by the scattered photons of the neutral hydrogen, rather than by the emitted photons by the absorbing gas.

6. Summary and Implications

In summary, the LoBAL quasar J1220+4549 shows abundant absorption lines, such as the HiBALs of C IV and Si IV and the LoBALs of Al III, C II, and Si III, as well as absorption from the Lyman series. The physical conditions of the absorber were probed by using absorption lines. The relations between N_H and (U and n_H) were established based on the measured $N_{H\,I}$, and the three parameters (U, n_H, and N_H) were determined jointly by using the measured column densities of the detected absorption lines and the photoionization simulations. We found that the absorbing gas is of high density at log n_H is 11.03 ± 0.50 cm^{-3}.

The distance of the absorber to the central BH was determined to be ∼0.3 pc, assuming solar abundance, which is one order of magnitude smaller than the sublimation radius of the dusty torus at $R_{sub} = 5.6$ pc. Therefore, the absorbing gas should not be from the dusty torus. By comparing the estimated r_{abs} and the location of the BLR, we think the absorber might be from the BLR. According to the estimated mass of the BH ($M_{BH} = 10^9 M_\odot$), the escape velocity at this location is calculated to be ∼13,849 km s^{-1}, which is about 69 times larger than the observed blueshifted velocity of the absorber. Thus, the absorber may be gas accumulated by the failed wind originating from the accretion disk.

One of the key findings of the work is that if other objects have a similar unsaturated Al III and small $N_{H\,I}$ like J1220+4549, their n_H will be quite high. In the future, H I and Al III absorption lines will be used to probe the nature of the absorbing gas in high-redshift quasars.

The authors thank the anonymous referee for the helpful suggestions. This work was jointly supported by the National Natural Science Foundation of China (NSFC 11503023) and the Shanghai Natural Science Foundation (grant Nos. 19ZR1462500 and 14ZR1444100). This work has made use of the data products of the SDSS and Catalina Sky Survey.

ORCID iDs

Qiguo Tian https://orcid.org/0000-0003-3495-5000
Xiheng Shi https://orcid.org/0000-0002-6710-7537
Zhenzhen Li https://orcid.org/0000-0002-8237-0237
Shaohua Zhang https://orcid.org/0000-0001-8485-2814
Hongyan Zhou https://orcid.org/0000-0003-1956-9021

References

Abazajian, K. N., Adelman-McCarthy, J. K., Agüeros, M. A., et al. 2009, ApJS, 182, 543
Arav, N., Borguet, B., Chamberlain, C., et al. 2013, MNRAS, 436, 3286
Arav, N., Kaastra, J., Kriss, G. A., et al. 2005, ApJ, 620, 665
Barvainis, R. 1987, ApJ, 320, 537
Bentz, M. C., Peterson, B. M., Netzer, H., et al. 2009, ApJ, 697, 160
Borguet, B. C. J., Edmonds, D., Arav, N., Dunn, J., & Kriss, G. A. 2012a, ApJ, 751, 107
Borguet, B. C. J., Edmonds, D., Arav, N., et al. 2012b, ApJ, 758, 69
Chamberlain, C., & Arav, N. 2015, MNRAS, 454, 675
Chen, C., Hamann, F., & Ma, B. 2021, ApJ, 909, 208
Clavel, J., Reichert, G. A., Alloin, D., et al. 1991, ApJ, 366, 64
Dawson, K. S., Schlegel, D. J., Ahn, C. P., et al. 2013, AJ, 145, 10
Dunn, J. P., Bautista, M., Arav, N., et al. 2010, ApJ, 709, 611
Elvis, M. 2000, ApJ, 545, 63
Elvis, M., Wilkes, B. J., McDowell, J. C., et al. 1994, ApJS, 95, 1
Ferland, G. J., Chatzikos, M., Guzmán, F., et al. 2017, RMxAA, 53, 385
Ferland, G. J., Korista, K. T., Verner, D. A., et al. 1998, PASP, 110, 761
Finn, C. W., Morris, S. L., Crighton, N. H. M., et al. 2014, MNRAS, 440, 3317
Fitzpatrick, E. L., & Massa, D. 2007, ApJ, 663, 320
Hall, P. B., Anderson, S. F., Strauss, M. A., et al. 2002, ApJS, 141, 267
Hamann, F. 1998, ApJ, 500, 798
Hamann, F., Barlow, T. A., Junkkarinen, V., et al. 1997, ApJ, 478, 80
Hamann, F., & Sabra, B. 2004, in ASP Conf. Ser. 311: AGN Physics with the Sloan Digital Sky Survey (San Francisco, CA: ASP), 203
Hamann, F., Tripp, T. M., Rupke, D., et al. 2019, MNRAS, 487, 5041
Hopkins, P. F., Hernquist, L., Cox, T. J., et al. 2006, ApJS, 163, 1
Ji, T., Zhou, H., Jiang, P., et al. 2015, ApJ, 800, 56
Kaspi, S., Brandt, W. N., Maoz, D., et al. 2007, ApJ, 659, 997
Kaspi, S., Maoz, D., Netzer, H., et al. 2005, ApJ, 629, 61
Kim, T.-S., Hu, E. M., Cowie, L. L., et al. 1997, AJ, 114, 1
Kishimoto, M., Hönig, S. F., Beckert, T., et al. 2007, A&A, 476, 713
Leighly, K. M., Dietrich, M., & Barber, S. 2011, ApJ, 728, 94
Lira, P., Kaspi, S., Netzer, H., et al. 2018, ApJ, 865, 56
Liu, W.-J., Zhou, H., Ji, T., et al. 2015, ApJS, 217, 11
Liu, W.-J., Zhou, H.-Y., Jiang, N., et al. 2016, ApJ, 822, 64
Lu, H., Wang, T., Yuan, W., et al. 2008, ApJ, 680, 858
Lynden-Bell, D. 1969, Natur, 223, 690
Lynds, C. R. 1967, ApJ, 147, 396
Lynds, R. 1971, ApJL, 164, L73
Mathews, W. G., & Ferland, G. J. 1987, ApJ, 323, 456
Matsuoka, Y., Kawara, K., & Oyabu, S. 2008, ApJ, 673, 62
Meijerink, R., Spaans, M., & Israel, F. P. 2007, A&A, 461, 793
Miller, T. R., Arav, N., Xu, X., et al. 2018, ApJ, 865, 90
Negrete, C. A., Dultzin, D., Marziani, P., et al. 2012, ApJ, 757, 62
Netzer, H. 2013, The Physics and Evolution of Active Galactic Nuclei (Cambridge: Cambridge Univ. Press)
Netzer, H. 2015, ARA&A, 53, 365
Netzer, H. 2020, MNRAS, 494, 1611
Panda, S., Czerny, B., Adhikari, T. P., et al. 2018, ApJ, 866, 115
Peterson, B. M. 1993, PASP, 105, 247
Peterson, B. M. 2006, Physics of Active Galactic Nuclei at All Scales (Berlin: Springer), 77
Quera-Bofarull, A., Done, C., Lacey, C., et al. 2020, MNRAS, 495, 402
Rees, M. J. 1984, ARA&A, 22, 471

Risaliti, G., & Elvis, M. 2010, A&A, 516, A89
Różańska, A., Nikołajuk, M., Czerny, B., et al. 2014, NewA, 28, 70
Runnoe, J. C., Brotherton, M. S., & Shang, Z. 2012, MNRAS, 422, 478
Savage, B. D., & Sembach, K. R. 1991, ApJ, 379, 245
Schlegel, D. J., Finkbeiner, D. P., & Davis, M. 1998, ApJ, 500, 525
Schneider, P. 2015, Extragalactic Astronomy and Cosmology: An Introduction (Berlin: Springer-Verlag)
Shi, X., Zhou, H., Shu, X., et al. 2016a, ApJ, 819, 99
Shi, X.-H., Jiang, P., Wang, H.-Y., et al. 2016b, ApJ, 829, 96
Tian, Q., Shi, X., Lu, H., et al. 2019, ApJ, 877, 72
Vanden Berk, D. E., Richards, G. T., Bauer, A., et al. 2001, AJ, 122, 549
Veilleux, S., Meléndez, M., Tripp, T. M., et al. 2016, ApJ, 825, 42
Vestergaard, M., & Peterson, B. M. 2006, ApJ, 641, 689
Weymann, R. J., Carswell, R. F., & Smith, M. G. 1981, ARA&A, 19, 41
Weymann, R. J., Morris, S. L., Foltz, C. B., et al. 1991, ApJ, 373, 23
Xu, X., Arav, N., Miller, T., et al. 2018, ApJ, 858, 39
Xu, X., Arav, N., Miller, T., et al. 2019, ApJ, 876, 105
York, D. G., Adelman, J., Anderson, J. E., Jr., et al. 2000, AJ, 120, 1579
Zamorani, G., Henry, J. P., Maccacaro, T., et al. 1981, ApJ, 245, 357
Zhang, S., Wang, T.-G., Wang, H., et al. 2010, ApJ, 714, 367
Zhang, S., Zhou, H., Shi, X., et al. 2015, ApJ, 815, 113
Zheng, W., Kriss, G. A., Telfer, R. C., Grimes, J. P., & Davidsen, A. F. 1997, ApJ, 475, 469
Zhou, H., Shi, X., Yuan, W., et al. 2019, Natur, 573, 83